A Novel All-Direction Antimisalignment Wireless Power Transfer System Designed by Truncated Region Eigenfunction Expansion Method

Zifan Dong, Xiaoming Li, Sheng Liu, Ziwei Xu, and Lin Yang

***Abstract*—This article proposes a novel wireless power transfer (WPT) system, which achieves high misalignment tolerance in all directions by using antiparallel windings. The transmitter coil is composed of two parts of wires wound in opposite directions; thus, the magnetic flux with different directions would counteract partly. With the properly designed parameters, the mutual inductance between transmitter and receiver coils could remain constant when misalignment occurs. Therefore, the output power and the efficiency of the system can remain unchanged. Moreover, this article proposes a novel analytical calculation method for mutual inductance based on the truncated region eigenfunction expansion method, which greatly promotes and simplifies the design process of a magnetic coupler. This method solves the problem of mutual inductance calculation with a finite ferrite substrate. Factors that influence the mutual inductance of circular coils are systematically studied based on the method. Finally, an experimental prototype is built to verify the validity of the system. The mutual inductance can remain 97% of the well-aligned value within a 0.1-m misalignment, and the overall efficiency is consistently higher than 90.2%, while the fluctuation of the output power is within 3%.**

***Index Terms*—Misalignment tolerance, mutual inductance, truncated region eigenfunction expansion (TREE), wireless power transfer (WPT).**

I. Introduction

WIRELESS power transfer (WPT) has become a popular research interest in recent years in both industry and academia [1]. Due to its superiority of convenience, flexibility, reliability, and security, it has aroused great attention in the field of power electronics. Nowadays, the WPT system has been successfully adopted in the applications of biomedical implants [2], LED lighting [3], electric vehicles (EVs) [4], underwater power supply [5], unmanned aerial vehicle (UAV) [6], and so on. Generally, lateral misalignment between the transmitter coil and the receiver coil will easily happen in practical applications, which has been a great challenge in WPT technology. Coil misalignment is an inherent problem of the WPT system, since the positions of the coils greatly influence the mutual inductance. Misalignment will lead to the decline of mutual inductance, which brings instability to the system and decreases the transfer efficiency [7]. Therefore, it is significant to design WPT systems with antimisalignment characteristics.

Various methods focusing on control strategies, topologies, and coil designs have been proposed to improve the misalignment performance of the WPT system. Some attempts on control schemes have been made in [8]–[11]. A novel phase-shift control method was proposed in [8] to achieve high misalignment tolerance. Liu *et al.* [9] proposed an active–reactive power (P–Q) based primary-side controller, which can regulate the output voltage with coil misalignment or load variations. The sliding-mode control [10] and proportional–integral–derivative (PID) control [11] can also be utilized to overcome the problem of misalignment. However, these methods require closed-loop controllers and communication devices, which increase the complexity of the system. The cost, volume, and loss of the system will increase simultaneously. The control system can be simplified, or even removed, if the WPT system is inherently antimisaligned. Therefore, other methods, e.g., topologies and coil designs, are studied to improve misalignment performance.

The compensation topology is another concern to solve the problem. With properly selected topologies and parameters, the misalignment tolerance of the WPT system can be improved. In [12], a series–parallel/series compensation topology was adopted to improve misalignment performance. A series/series–parallel compensation topology was proved to realize robust reaction to the coupling coefficient [13]. An optimized inductor–capacitor–capacitor (LCC) topology was proposed to achieve coupling-insensitive gain and output power [14]. Nevertheless, these methods can only reduce the output characteristics' sensitivity to the coupling coefficient or mutual inductance and, hence, reduce the fluctuation of output voltage/current and output power when misalignment occurs. However, they are still unable to keep constant. In some research, the hybrid topology was proposed to improve the misalignment tolerance; either coupled or decoupled coils can be used. Zhao *et al.* [15] proposed a hybrid LCC–LCC/series–series

Manuscript received March 31, 2021; accepted May 15, 2021. Date of publication May 21, 2021; date of current version July 30, 2021. This work was supported by the 2019 Nanning innovation and entrepreneurship leading talents "Yongjiang plan" funding project. Recommended for publication by Associate Editor M. Ponce-Silva. *(Corresponding author: Lin Yang.)*

Zifan Dong, Xiaoming Li, and Ziwei Xu are with the School of Electrical Engineering and Automation, Wuhan University, Wuhan 430072, China (e-mail: zifan_dong@whu.edu.cn; xmli@whu.edu.cn; Ziwei_xu@whu.edu.cn).

Sheng Liu is with the School of Electrical Engineering and Automation, Wuhan University, Wuhan 430072, China. He is now with the College of Electrical Engineering, Zhejiang University, Hangzhou 310027, China (e-mail: sheng_liu@zju.edu.cn).

Lin Yang was with the School of Electrical Engineering and Automation, Wuhan University, Wuhan 430072, China. He is now with the College of Electronic and Electrical Engineering, Henan Normal University, Xinxiang 453007, China (e-mail: yang_lin@whu.edu.cn).

Color versions of one or more figures in this article are available at https://doi.org/10.1109/TPEL.2021.3082777.

Digital Object Identifier 10.1109/TPEL.2021.3082777

(SS) topology using a combination of two different resonant networks to realize a constant output power and efficiency with misalignment. The coils in [15] can also be replaced by decoupled coils to achieve the same effect [16]. Similarly, an S-LCC/LCC-S topology was proposed in [17]. One-to-multiple [18] and multiple-to-one [19] WPT topologies being able to improve misalignment tolerance were also proposed. These systems can be regarded as two WPT systems (hybrid or separated) charging for one load together. They consume much more amount of copper, more passive components, and even more converters. Thus, the cost and power loss will increase.

Another solution is to design new structure coils. Traditionally, circular and square coils have been widely used in the WPT system. However, these two simple geometries are of low misalignment tolerance. Many magnetic couplers with new structures were proposed to improve misalignment tolerance [20]–[23]. A double D (DD) pad, which achieves the misalignment tolerance larger than traditional circular pads with similar size, was first proposed in [20]. Additional quadrature coils (referred as Q coil) were added to compose DDQ [16] and DD2Q [21] pads, which further improved the capability of antimisalignment. Other new structure pads such as bipolar [22] and Taichi pads [23] were also presented to obtain a larger misalignment tolerance. Nevertheless, these methods achieve high misalignment tolerance only in one direction, which limits their application.

Coil design is a significant part of the whole WPT system design. Mutual inductance is the most important parameter to be designed since it greatly influences the system performance. To date, coils are designed by a finite-element analysis (FEA) method in most cases. The calculation of mutual inductance relies on FEA simulation, which is tedious and complicated. The processes of 3-D modeling are arduous with heavy workload. Especially, in the studies on misalignment, in order to acquire the curve of mutual inductance versus misalignment, models of each design need to be simulated a large number of times.

Compared to the numerical methods, the analytical method is more convenient, flexible, and efficient. Hence, the analytical method of coil design in the WPT system gradually attracts more attention. In [24], the analytical formula to calculate the mutual inductance between noncoaxial coils was proposed using Bessel functions. Commonly, in WPT systems, ferrite substrates are utilized to enhance the mutual inductance. The calculation of mutual inductance with ferrite substrates has been analyzed in [25]–[28]. Research [25] presents an analytical solution to primary and secondary coils sandwiched by the ferrite substrate based on Fourier–Bessel transformation. The method was also used to give a solution to square coils in the same situation [26]. Su *et al.* [28] further derived the solution with double-layer substrates. However, all the aforementioned derivations are based on the assumption that the magnetic substrates are infinite in the radial direction. In usage, the outermost radius or width of the substrate should be at least twice larger than that of the coils to obtain a good approximation, which brings huge obstacles in practical application.

The traditional classical analytical method cannot give solutions to the situation with finite ferrite substrates, since there will be unsolvable transcendental integral equations in the process of solving the interface condition on radial direction. The truncated region eigenfunction expansion (TREE) method is a novel and powerful analytical method in solving electromagnetic field, which has been widely used in the area of eddy current testing [29], [30]. Same as the classical approach, separation of variables is used to obtain the analytical expression of electromagnetic field. Differently, the TREE method truncates the solution domain to a finite range; thus, the solution will be expressed in the form of series instead of integral. As a result, the transcendental integral equations turn to solvable algebraic equations.

In this article, a novel WPT system with all-direction antimisalignment characteristic is proposed. The transmitter coil consists of two parts of wires wound in opposite directions; then, the magnetic flux of different directions would counteract in part. As a result, the total mutual inductance between transmitter and receiver coils could remain constant when misalignment occurs. Therefore, the output current, power, and efficiency can remain unchanged, which brings great convenience to practical applications, simplifying or even canceling control schemes. Due to the axisymmetric shapes, the system can achieve high misalignment tolerance in full 360° range. Furthermore, this article presents a novel analytical calculation method for the mutual inductance based on the TREE method, which is extremely helpful to the design of the proposed antimisalignment WPT system. The method can accurately calculate the mutual inductance of circular coils with finite ferrite substrates. The factors that influence the mutual inductance of circular coils with finite ferrite substrate are systematically studied. Finally, an experimental prototype was established to verify the validity and feasibility of the proposed system. The system can be widely used in the cases where the position of load is not fixed, e.g., EVs, biomedical implants, and consumer electronics. Considering the axisymmetric antimisalignment characteristic, the system is very suitable for charging the drones, since the landing error of a drone can occur in every direction.

The remainder of this article is organized as follows. Section II establishes a mathematical model of the proposed WPT system. The novel analytical calculation method for the mutual inductance is derived in Section III. In Section IV, a comprehensive analysis of the mutual inductance is demonstrated. Section V proposes a methodology for system design and Section VI verifies the antimisalignment characteristic of the proposed system with the experiment. Finally, Section VII concludes this article.

II. System Modeling and Analysis

Fig. 1 shows the prototype of the proposed all-direction antimisalignment WPT system, which consists of a dc voltage source, a full-bridge inverter, a magnetic coupler, a full-bridge rectifier, and a load. In this section, the first harmonic approximation method is utilized to analyze the system. The fundamental component of the output voltage of the inverter is deduced as

$$u_1(t) = \frac{4}{\pi} U_{\text{in}} \sin \omega t \tag{1}$$

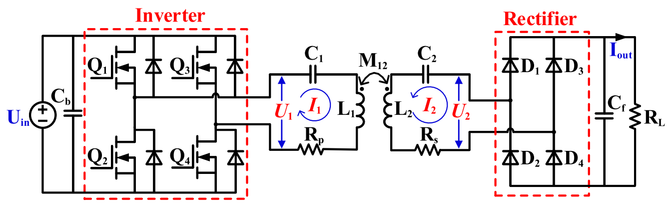

Fig. 1. Circuit diagram of the proposed all-range antimisalignment WPT system.

where U_{in} denotes the input voltage, ω is the operating angular frequency, and $\omega = 2\pi f$.

Therefore, the phasor form of u_1 can be written as

$$\dot{U}_1 = \frac{2\sqrt{2}}{\pi} U_{\text{in}} \angle 0. \tag{2}$$

Then, the circuit equation can be obtained according to Kirchhoff's law as follows:

$$\begin{cases} \dot{U}_1 = (j\omega L_1 + \frac{1}{j\omega C_1} + R_p)\dot{I}_1 - j\omega M_{12}\dot{I}_2 \\ 0 = -j\omega M_{12}\dot{I}_1 + (j\omega L_2 + \frac{1}{j\omega C_2} + R_s + R_{\text{eq}})\dot{I}_2 \end{cases} \tag{3}$$

where L_1 and L_2 denote the self-inductance of the transmitter and receiver coils, respectively. C_1 and C_2 denote the corresponding compensation capacitors. R_p and R_s denote the equivalent series resistance (ESR) of primary and secondary coils, respectively. M_{12} is the mutual inductance between the two coils, and R_{eq} is the equivalent resistance of the rectifier and the load.

The topology of the system is chosen as SS compensation for the sake of simplicity, and the SS topology can achieve both constant-current output and zero-phase-angle condition [31]. In the system, each coil is of the same resonate angular frequency $\omega = \frac{1}{\sqrt{L_1 C_1}} = \frac{1}{\sqrt{L_2 C_2}}$. Then, the circuit equation can be simplified as

$$\begin{cases} \dot{U}_1 = R_p \dot{I}_1 - j\omega M_{12}\dot{I}_2 \\ 0 = -j\omega M_{12}\dot{I}_1 + (R_s + R_{\text{eq}})\,\dot{I}_2. \end{cases} \tag{4}$$

Thus, $\dot{I}_1$ and $\dot{I}_2$ can be solved as

$$\begin{cases} \dot{I}_1 = \dfrac{(R_s + R_{\text{eq}})\dot{U}_1}{\omega^2 M^2 + R_p R_{\text{eq}} + R_p R_s} \\ \dot{I}_2 = \dfrac{j\omega M \dot{U}_1}{\omega^2 M^2 + R_p R_{\text{eq}} + R_p R_s}. \end{cases} \tag{5}$$

Assuming that the power loss of the rectifier is neglected, the equivalent resistance R_{eq} and the output current I_{out} can be deduced as

$$R_{\text{eq}} = \frac{8}{\pi^2} R_L \tag{6}$$

$$I_{\text{out}} = \frac{2\sqrt{2}}{\pi} \left| \dot{I}_2 \right| \tag{7}$$

where $|\dot{I}_2|$ denotes the modulus of $\dot{I}_2$ [32].

Then, the efficiency from the output of the inverter to the load can be calculated as

$$\eta = \frac{\left|\dot{I}_2\right|^2 R_{\text{eq}}}{\text{Re}(\dot{U}_1 \dot{I}_1)} = \frac{\omega^2 M^2 R_{\text{eq}}}{(R_s + R_{\text{eq}})(\omega^2 M^2 + R_p R_{\text{eq}} + R_p R_s)} \tag{8}$$

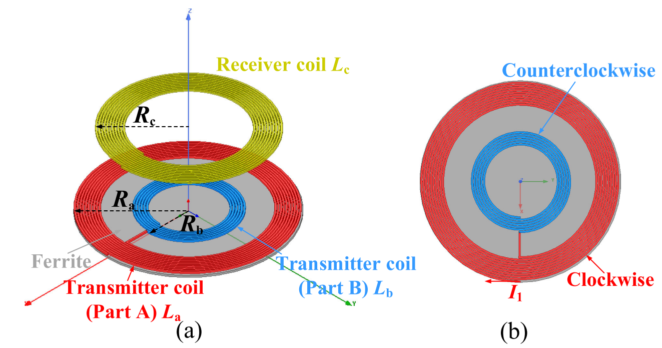

Fig. 2. Structure of the proposed magnetic coupler. (a) Overview. (b) Transmitter coil.

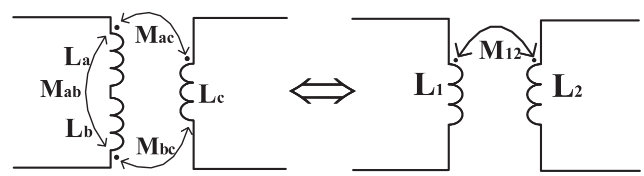

Fig. 3. Equivalent circuit diagram of the magnetic coupler.

where Re denotes the real part of a phasor.

In this article, the antimisalignment characteristic is the inherent property of the system. It depends on the magnetic coupler rather than the circuit topology or the control scheme. Thus, it is significant to properly design the magnetic coupler.

The structure of the proposed magnetic coupler is shown in Fig. 2. The magnetic coupler is composed of a transmitter coil L_1 in the primary side and a receiver coil L_2 in the secondary side. The coils and the ferrite are all designed as circular shape in order to obtain the axisymmetric property. The transmitter coil consists of two parts of wires wound in opposite directions (clockwise and counterclockwise), as is shown in red and blue in Fig. 2. Wires with different winding directions will produce magnetic flux with opposite directions according to Lenz's law. Therefore, the transmitter coil can be regarded as two single coil series reversely. The equivalent circuit diagram of the magnetic coupler is shown in Fig. 3.

In Fig. 3, L_a and L_b denote the turns with different winding directions in the transmitter coil. According to the Kirchhoff voltage law, the self-inductance and the mutual inductance between the two coils can be calculated as

$$L_1 = L_a + L_b - 2M_{ab} \tag{9}$$

$$L_2 = L_c \tag{10}$$

$$M_{12} = M_{ac} - M_{bc}. \tag{11}$$

When misalignment occurs, M_{ac} and M_{bc} will decrease simultaneously. The antimisalignment characteristic can be obtained if the magnitudes of the decline ΔM_{ac} and ΔM_{bc} are the same, i.e., the difference between M_{ac} and M_{bc} remains constant. Then, the mutual inductance between primary and secondary coils, M_{12}, will remain unchanged. Therefore, the key point is to study the curve of mutual inductance versus misalignment.

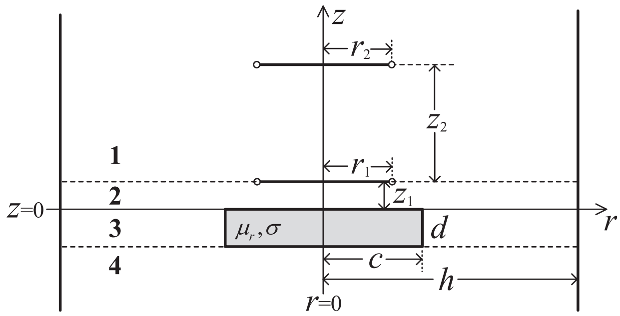

Fig. 4. Cross-sectional axisymmetric view of a filamentary coil above a finite ferrite substrate.

III. Analytical Derivation

In this section, the TREE method is utilized to obtain the analytical solution of the time-harmonic electromagnetic field and then calculate the mutual inductance between planar circular coils with a finite ferrite substrate.

A. Coaxial Filamentary Coils

Considering the axisymmetric geometries, the cylindrical coordinate system (r, φ, z) is established instead of the Cartesian one (x, y, z). The cross-sectional axisymmetric view of two filamentary coils above a finite ferrite substrate and the geometric parameters is shown in Fig. 4. The primary coil with the radius r_1 is placed on a linear, homogeneous, and isotropic circular ferrite substrate with the relative magnetic permeability μ_r and conductivity σ. The radius and thickness of the ferrite substrate are c and d, respectively. The primary coil is excited by steady-state sinusoidal current $Ie^{j\omega t}$.

The solution domain is truncated in the form of a cylinder at $r = h$. The domain is divided into four regions separated by the planes $z = z_1$, $z = 0$, and $z = -d$, denoted as regions 1, 2, 3, and 4. The magnetic vector potential $\mathbf{A}$ with the Lorenz gauge is introduced in order to facilitate the analysis. Therefore, the magnetic flux density $\mathbf{B}$ and the magnetic field strength $\mathbf{H}$ can be calculated as

$$\begin{cases} \mathbf{B} = \nabla \times \mathbf{A} \\ \mathbf{H} = \mu \cdot \nabla \times \mathbf{A} \end{cases} \tag{12}$$

where ∇ denotes the nabla operator and μ denotes the magnetic permeability.

It is proved that the magnetic vector potential $\mathbf{A}$ has only circumferential component, i.e., $\mathbf{A} = A \cdot \vec{e_\varphi}$, in the axisymmetric time-harmonic electromagnetic field [33]. Deduced from Maxwell's equations, the magnitude of magnetic vector potential in each region $\mathbf{A}_\alpha$ $(\alpha = 1, 2, 3, 4)$ satisfies the following constraint equation:

$$\nabla^2 \mathbf{A}_\alpha + ({k_\alpha}^2 - \frac{1}{r^2})\mathbf{A}_\alpha = 0 \tag{13}$$

where $k_1 = k_2 = k_4 = 0$ and ${k_3}^2 = -j\omega\mu_0\mu_r\sigma$ [29], [33]. ∇^2 denotes the Laplace operator.

The partial differential equation (13) can be solved by the method of variable separation. It can be solved in the form of integral [33], [34] or in the form of series [29]. According to the TREE method, the general solution of (13) can be written as

$$A(r, z) = \sum_{i=1}^{\infty} [A_i J_1(k_i r) + B_i Y_1(k_i r)] \cdot \left[C_i e^{\lambda_i z} + D_i e^{-\lambda_i z}\right] \tag{14}$$

where k_i is an eigenvalue and $\lambda_i = \sqrt{{k_i}^2 + j\omega\mu_0\mu_r\sigma}$. A_i, B_i, C_i, and D_i are unknown coefficients determined by interface conditions. $J_1(x)$ and $Y_1(x)$ denotes the Bessel function of the first and the second kind, respectively [35]. They have the following properties [36]:

$$\begin{gathered} \lim_{x\to 0} J_1(x) = 0, \lim_{x\to\infty} |J_1(x)| = 0 \\ \lim_{x\to 0} |Y_1(x)| = \infty, \lim_{x\to\infty} |Y_1(x)| = 0. \end{gathered} \tag{15}$$

Note that the magnetic vector potential at $r = 0$ should be finite. Due to the divergence of $Y_1(x)$ at the origin, B_i should be set as 0. Therefore, $A(r, z)$ in regions 1, 2, and 4 can be deduced as

$$A_1(r, z) = \sum_{i=1}^{\infty} J_1(k_i r) e^{-k_i z} {D_i}^{(1)} \tag{16}$$

$$A_2(r, z) = \sum_{i=1}^{\infty} J_1(k_i r)(e^{k_i z} {C_i}^{(2)} + e^{-k_i z} {D_i}^{(2)}) \tag{17}$$

$$A_4(r, z) = \sum_{i=1}^{\infty} J_1(k_i r) e^{k_i z} {C_i}^{(4)}. \tag{18}$$

According to the TREE method, the Dirichlet condition is applied to the boundary, which means that the magnetic vector potential vanishes at $r = h$, i.e., $A(h, z) = 0$. Thus, the eigenvalues k_i can be solved from the equation $J_1(k_i h) = 0$.

Region 3 includes two subregions: the ferrite and the air. According to the method of variable separation, the general solution of $A(r, z)$ consists of two parts, which are the functions of r and z:

$$R(r) = AJ_1(qr) + BY_1(qr) \tag{19}$$

$$Z(z) = Ce^{pz} + De^{-pz} \tag{20}$$

where the eigenvalues are q and $p = \sqrt{q^2 + j\omega\mu_0\mu_r\sigma}$. In order to construct a solution for the air subregion, one can replace q by p in $R(r)$ or replace p by q in $Z(z)$; in either case, Laplace's equation for the magnetic vector potential in air is satisfied [29]. The former one is chosen, making the z-dependence solution $Z(z)$ of the air region conform to that of the ferrite region. The expressions for the two subregions are then written as

$$A_3^{fer}(r, z) = \sum_{i=1}^{\infty} J_1(q_i r)(e^{p_i z} {C_i}^{(3)} + e^{-p_i z} {D_i}^{(3)}) \tag{21}$$

$$\begin{aligned} A_3^{air}(r, z) = \sum_{i=1}^{\infty} & [({A_i}^{(3)} J_1(p_i r) + {B_i}^{(3)} Y_1(p_i r)) \cdot \\ & (e^{p_i z} {C_i}^{(3)} + e^{-p_i z} {D_i}^{(3)})]. \end{aligned} \tag{22}$$

Due to the continuity of the normal component of $\mathbf{B}$ and the tangential component of $\mathbf{H}$, the interface condition on the interface $r = c$ can be shown as

$$J_1(q_i c) = A_i J_1(p_i c) + B_i Y_1(p_i c) \tag{23}$$

$$\frac{1}{\mu_r} q_i J_0(q_i c) = A_i p_i J_0(p_i c) + B_i p_i Y_0(p_i c). \tag{24}$$

Thus, the coefficients A_i and B_i can be solved as

$$A_i = \frac{-\frac{1}{\mu_r} q_i J_0(q_i c) Y_1(p_i c) + p_i J_1(q_i c) Y_0(p_i c)}{p_i J_1(p_i c) Y_0(p_i c) - p_i J_0(p_i c) Y_1(p_i c)} \tag{25}$$

$$B_i = \frac{\frac{1}{\mu_r} q_i J_0(q_i c) J_1(p_i c) - p_i J_1(q_i c) J_0(p_i c)}{p_i J_1(p_i c) Y_0(p_i c) - p_i J_0(p_i c) Y_1(p_i c)}. \tag{26}$$

Note that $R(p_i r) = A_i J_1(p_i r) + B_i Y_1(p_i r)$; then, $A_3^{\text{air}}(r, z)$ can be rewritten as

$$A_3^{\text{air}}(r, z) = \sum_{i=1}^{\infty} R(p_i r)(e^{p_i z} C_i{}^{(3)} + e^{-p_i z} D_i{}^{(3)}). \tag{27}$$

Therefore, the eigenvalues p_i and q_i can be solved similarly by $R(p_i h) = 0$.

According to the interface conditions, B_z and H_r are continuous at the horizontal interfaces $z = z_0$, $z = 0$, and $z = -d$. Thus, it can be obtained that

$$A_1(r, z_1) = A_2(r, z_1) \tag{28}$$

$$\left.\frac{\partial A_1(r,z)}{\partial z}\right|_{z=z_1} - \left.\frac{\partial A_2(r,z)}{\partial z}\right|_{z=z_1} = -\mu_0 I \delta(r - r_0) \tag{29}$$

$$A_2(r, 0) = A_3(r, 0) \tag{30}$$

$$\left.\frac{\partial A_2(r,z)}{\partial z}\right|_{z=0} = \frac{1}{\mu_r}\left.\frac{\partial A_3(r,z)}{\partial z}\right|_{z=0} \tag{31}$$

$$A_3(r, -d) = A_4(r, -d) \tag{32}$$

$$\frac{1}{\mu_r}\left.\frac{\partial A_3(r,z)}{\partial z}\right|_{z=-d} = \left.\frac{\partial A_4(r,z)}{\partial z}\right|_{z=-d}. \tag{33}$$

Although the complete solution is an infinite series, practically, only a finite number of summation terms n are needed for a good approximation of the solution, due to the quick convergence of the series [29]. In order to simplify the derivation, expressions of $A(r, z)$ can be rewritten in the form of matrix. Take $A_1(r, z)$ as an example

$$A_1(r, z) = \sum_{i=1}^{n} J_1(k_i r) e^{-k_i z} D_i{}^{(1)} = J_1(\mathbf{k}^{\mathrm{T}} r) e^{-\mathbf{k} z} \mathbf{D}^{(1)} \tag{34}$$

where

$$J_1(\mathbf{k}^{\mathrm{T}} r) = [\, J_1(k_1 r)\ J_1(k_2 r) \cdots J_1(k_n r) \,]$$
$$e^{\mathbf{k}z} = \begin{bmatrix} e^{k_1 z} & 0 & \cdots & 0 \\ 0 & e^{k_2 z} & \cdots & 0 \\ \vdots & \vdots & \ddots & \vdots \\ 0 & 0 & \cdots & e^{k_n z} \end{bmatrix}, \mathbf{D}^{(1)} = \begin{bmatrix} D_1^{(1)} \\ D_2^{(1)} \\ \vdots \\ D_n^{(1)} \end{bmatrix}. \tag{35}$$

Multiplying each side of the above equations with $J_1(\mathbf{k}^{\mathrm{T}} r)$, integrating from 0 to h with respect to r, and using the orthogonality property of the Bessel function, we obtain

$$\int_0^h J_1(k_i r) J_1(k_i r) r dr = \begin{cases} 0, i \neq j \\ \dfrac{[h J_0(k_i h)]^2}{2}, i = j \end{cases}. \tag{36}$$

Then, (28) becomes

$$e^{-\mathbf{k} z_0} \mathbf{D}^{(1)} = e^{\mathbf{k} z_0} \mathbf{C}^{(2)} + e^{-\mathbf{k} z_0} \mathbf{D}^{(2)}. \tag{37}$$

Similarly, (29)–(33) can be rewritten as

$$-\mathbf{E}\mathbf{k} e^{-\mathbf{k} z_0} \mathbf{D}^{(1)} = \mathbf{E}\mathbf{k}(e^{\mathbf{k} z_1} \mathbf{C}^{(2)} - e^{-\mathbf{k} z_1} \mathbf{D}^{(2)}) - \mu_0 I r_1 J_1(\mathbf{k} r_1) \tag{38}$$

$$\mathbf{E}(\mathbf{C}^{(2)} + \mathbf{D}^{(2)}) = \mathbf{U}(\mathbf{C}^{(3)} + \mathbf{D}^{(3)}) \tag{39}$$

$$\mathbf{E}\mathbf{k}(\mathbf{C}^{(2)} - \mathbf{D}^{(2)}) = \mathbf{V}\mathbf{p}(\mathbf{C}^{(3)} - \mathbf{D}^{(3)}) \tag{40}$$

$$\mathbf{U}(e^{-\mathbf{k}d} \mathbf{C}^{(3)} + e^{\mathbf{k}d} \mathbf{D}^{(3)}) = \mathbf{E} e^{-\mathbf{k}d} \mathbf{C}^{(4)} \tag{41}$$

$$\mathbf{V}\mathbf{p}(e^{-\mathbf{k}d} \mathbf{C}^{(3)} - e^{\mathbf{k}d} \mathbf{D}^{(3)}) = \mathbf{E}\mathbf{k}\mathbf{C}^{(4)} \tag{42}$$

where

$$J_1(\mathbf{k} r_1) = [\, J_1(k_1 r_1)\ J_1(k_2 r_1) \cdots J_1(k_n r_1) \,]^{\mathrm{T}} \tag{43}$$

$$\mathbf{E}_{ij} = \int_0^h J_1(k_i r) J_1(k_j r) r dr = \delta_{ij} \frac{[h J_0(k_i h)]^2}{2} \tag{44}$$

$$\mathbf{U}_{ij} = \int_0^c J_1(k_i r) J_1(q_j r) r dr + \int_c^h J_1(k_i r) R_1(p_j r) r dr \tag{45}$$

$$\mathbf{V}_{ij} = \frac{1}{\mu_r} \int_0^c J_1(k_i r) J_1(q_j r) r dr + \int_c^h J_1(k_i r) R_1(p_j r) r dr. \tag{46}$$

δ_{ij} is the Kronecker symbol. $\mathbf{k}$, $\mathbf{p}$, $e^{-\mathbf{k} z_1}$, $e^{\mathbf{k} z_1}$, $e^{-\mathbf{k}d}$, and $e^{\mathbf{k}d}$ are nth-order diagonal matrices. $\mathbf{D}^{(1)}$, $\mathbf{C}^{(2)}$, $\mathbf{D}^{(2)}$, $\mathbf{C}^{(3)}$, $\mathbf{D}^{(3)}$, and $\mathbf{C}^{(4)}$ are column vectors.

The matrix equations (38)–(42) can be solved symbolically by hand or numerically by computing software MATLAB or Mathematica. Here, we only concentrate on the magnetic field in region 1. Once the coefficients $\mathbf{D}^{(1)}$ are solved out, the magnetic flux can be calculated by Neumann's formula $\Phi_{12} = \oint_{l_2} A_1(r_2, z_2) \cdot dl_2$. Then, the mutual inductance can be derived as

$$M_{12} = \frac{\Phi_{12}}{I} = \frac{2\pi r_2}{I} \sum_{i=1}^{n} J_1(k_i r) e^{-k_i z} D_i{}^{(1)}. \tag{47}$$

Note that the current I can be canceled out since there is a coefficient $\mu_0 I r_1$ in $D_i{}^{(1)}$.

B. Noncoaxial Filamentary Coils

For the case of two noncoaxial filamentary coils, the mutual inductance can be calculated in the same way by Neumann's formula. Fig. 5 illustrates the top view of two misaligned filamentary coils, and the ferrite substrate is omitted. The magnetic field generated by the transmitter coil will not be altered by the

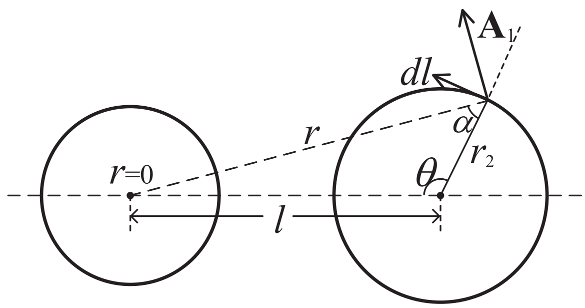

Fig. 5. Top view of two noncoaxial circular filamentary coils.

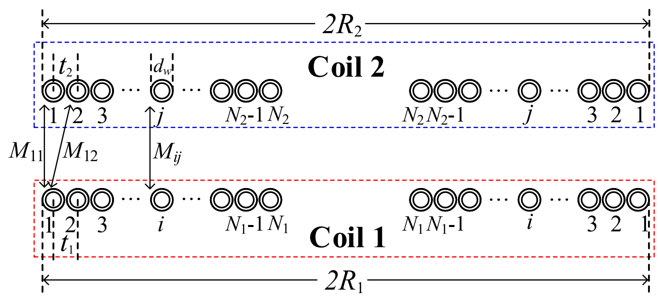

Fig. 6. Cross-sectional view of two multiturn planar spiral coils.

movement of the receiver coil. The magnetic vector potential in region 1 is the same as the well-aligned case. Similarly, the mutual inductance is derived as

$$\begin{aligned} M_{12} &= \frac{1}{I}\oint_{l_2} A_1(r,z_2)\cdot dl_2 = \frac{1}{I}\int_0^{2\pi} A_1(r,z_2)\cdot\cos\alpha r_2 d\theta \\ &= \frac{1}{I}\int_0^{2\pi}\left[\sum_{i=1}^{n} J_1(k_i r)e^{-k_i z_2}D_i^{(1)}\right]\frac{r_2 - l\cos\theta}{r}r_2 d\theta \\ &= 2\sum_{i=1}^{n}\int_0^{\pi}\left[J_1(k_i r)e^{-k_i z_2}\frac{D_i^{(1)}}{I}\frac{r_2 - l\cos\theta}{r}r_2\right]d\theta \end{aligned} \tag{48}$$

where $r = \sqrt{l^2 + r_2{}^2 - 2lr_2\cos\theta}$. When $l = 0$, (48) reduces to (47).

C. Multiturn Coils

Fig. 6 shows the cross-sectional view of the multiturn planar spiral coils. Based on the derivation on filamentary coils, the mutual inductance between two multiturn coils can be calculated by the superposition principle [37]. The outer diameter of the coil is much larger than the turn space. Therefore, the spiral coil can be regarded as several concentric circular filamentary coils in series. For a primary coil with N_1 turns and a secondary coil with N_2 turns, the mutual inductance can be calculated as

$$M = \sum_{i=1}^{N_1}\sum_{j=1}^{N_2} M_{ij} \tag{49}$$

where M_{ij} denotes the mutual inductance between two single loops, as shown in Fig. 6. The radius of each coil r_i and r_j can

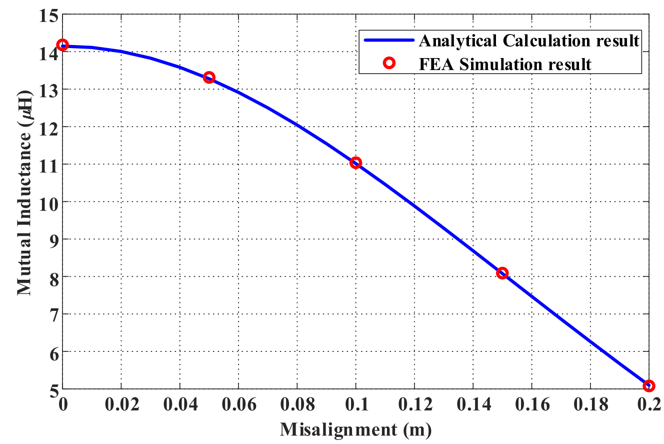

Fig. 7. Verification of the analytical method by FEA simulation.

be calculated as

$$r_i = R_1 - t_1(i-1) - \frac{d_w}{2}, \quad i = 1, 2, \ldots, N_1 \tag{50}$$

$$r_j = R_2 - t_2(j-1) - \frac{d_w}{2}, \quad j = 1, 2, \ldots, N_2 \tag{51}$$

where d_w denotes the wire diameter. Then, M_{ij} can be calculated by substituting r_i and r_j into (48).

D. Simulation Verification

To verify the validity of proposed formulas, FEA simulation software Ansoft Maxwell is used to calculate the mutual inductance in the same case with analytical calculation by MATLAB. In the example, the radius of the coils is set equally as 0.2 m, i.e., $R_1 = R_2 = 0.2$ m. The numbers of turns are $N_1 = N_2 = 10$. The turn spaces are $t_1 = t_2 = 4.8$ mm. The distance between the transmitter coil and the upper surface of the ferrite substrate is $z_1 = 2.6$ mm. The distance between two coils is $z_2 = 15$ cm. The radius and the thickness of the ferrite c and d are 0.2 m and 4 mm, respectively. $\mu_r = 2300$, $\sigma = 0.001$ S/m, and $f = 85$ kHz. The wire diameter is $d_w = 3.2$ mm. The calculation results compared with FEA simulation results are shown in Fig. 7.

The simulation results are in good agreement with the analytical results, which verifies the validity of the analytical derivation and the proposed formula.

IV. Analysis of Mutual Inductance

As shown in Fig. 7, with the receiver coil moving away from the well-aligned position, the curve of mutual inductance versus misalignment shows a downward trend. In order to find two curves with identical shape, i.e., the two curves are approximately parallel, factors that affect the shape of the mutual inductance curve should be fully studied.

In this section, the influence of outer radius, number of turns, and turn space of the transmitter coil on the mutual inductance is analyzed. The study is carried out by making one of the parameters as a variable, as shown in Table I. The other parameters are

TABLE I
PARAMETERS OF THE TESTED CALCULATION EXAMPLES

	Outer radius R_1	Number of turns N_1	Turn space t_1
Test 1	0.20m,0.18m,0.16m,0.14m	10	4.8mm
Test 2	0.2m	5,10,15,20	4.8mm
Test 3	0.2m	10	3.2mm,4.8mm,6.0mm,7.2mm

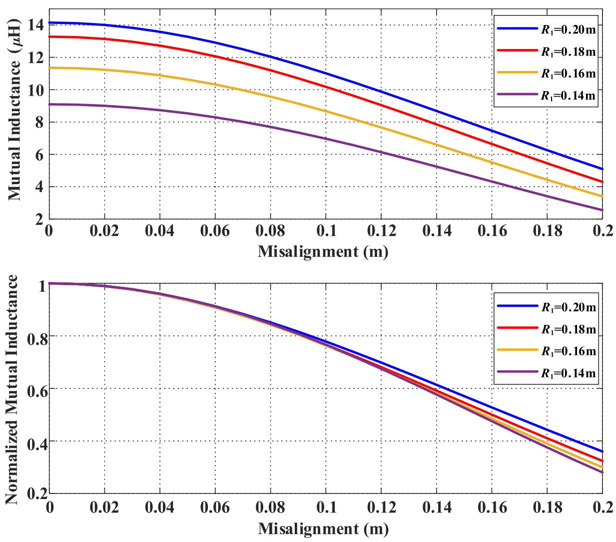

Fig. 8. Mutual inductance versus lateral misalignment among different outer radius R_2 ($R_2 = 20$ cm, $N_1 = N_2 = 10$, and $t_1 = t_2 = 4.8$ mm).

the same as those in the calculation example in Section III. The analysis can provide guidance to the coil design in next section.

A. Outer Radius

Fig. 8 shows the curve of mutual inductance versus lateral misalignment among different outer radius R_1, and it ranges from 0.05 to 0.20 m, while $R_2 = 0.2$ m, $N_2 = 10$, and $t_2 = 4.8$ mm. The mutual inductance results are also normalized with the well-aligned value ($M|_{l=0}$) for clearer comparison. It can be seen from Fig. 8 that the mutual inductance increases with the enlargement of R_1, which is consistent with equation (48). Expanding outer radius will decrease the curve's rate of descent, making the curve smoother.

B. Number of Turns

The second test is carried out with different number of turns of the transmitter coil, and the result is shown in Fig. 9. According to (49), the mutual inductance becomes larger when the number of turns increases, as demonstrated in Fig. 9. In practical applications, the size and geometrical dimension of the coils are usually under various restrictions, which brings obstacles to the coil design. Therefore, increasing the number of turns instead of enlarging coil radius becomes an effective way to improve the mutual inductance under these circumstances. In addition, on the contrary with expanding outer radius, increasing the number of turns will steepen the curve.

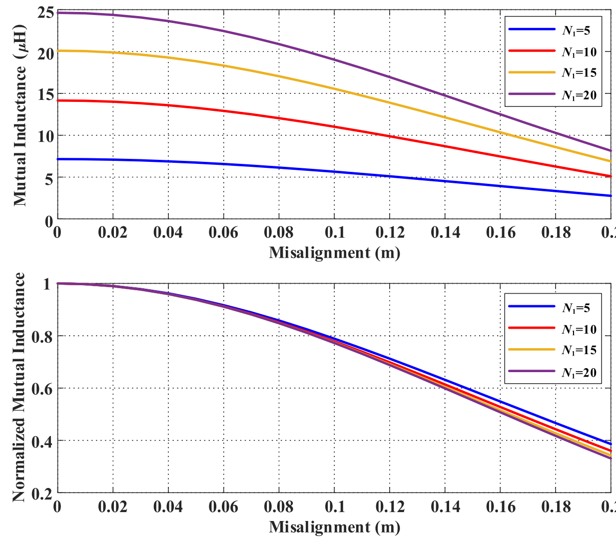

Fig. 9. Mutual inductance versus lateral misalignment among different number of turns N_1 ($R_1 = R_2 = 20$ cm, $N_2 = 10$, and $t_1 = t_2 = 4.8$ mm).

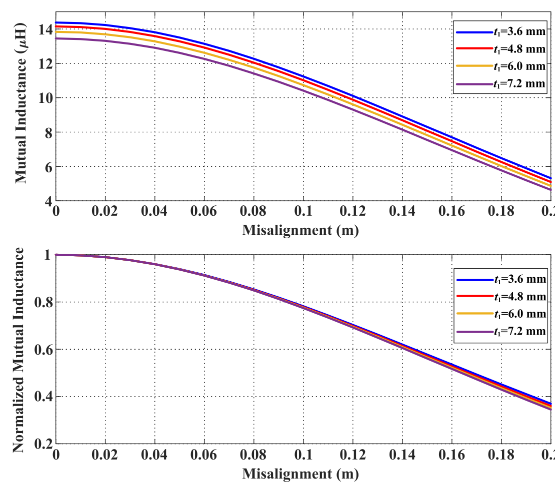

Fig. 10. Mutual inductance versus lateral misalignment among different turn space t_1 ($R_1 = R_2 = 20$ cm, $N_1 = N_2 = 10$, and $t_2 = 4.8$ mm).

C. Turn Space

As shown in Fig. 6, turn space t_1 actually affects the radius of each filamentary loop in the spiral coil. Fig. 10 illustrates that the mutual inductance descends with the increase in turn space. The influence of turn space on the mutual inductance is not significant compared to the aforementioned factors. It should be noted that the ESR of the coil increases with the decline of turn space due to skin effect and proximity effect, which may reduce the power transfer efficiency [38]. However, the increase in turn space will obviously enlarge the volume of the coils, leading to a low energy density of the system and inconvenience in practical application.

V. DESIGN OF THE MAGNETIC COUPLER

With the derived formula in Section III and the analysis in Section IV, the required magnetic coupler can be easily designed. The analytical formula greatly reduces the workload

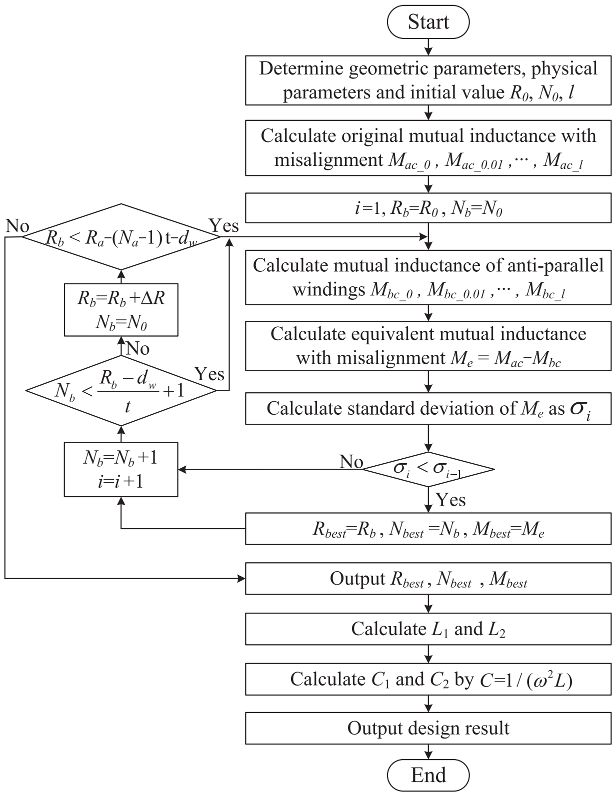

Fig. 11. Flowchart for the design process of the magnetic coupler.

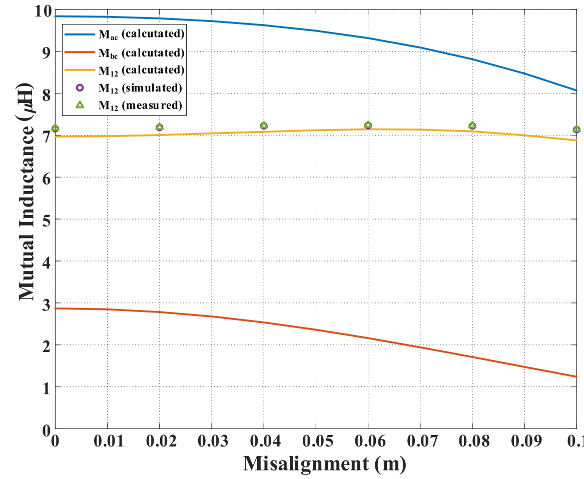

Fig. 12. Mutual inductances versus misalignment of the designed magnetic coupler.

of coil design and makes it possible to design automatically by program in computing software instead of FEA simulation software.

In practical application, the size of the transmitter coil and the receiver coil is under various restrictions according to uses, environment, and structure. Therefore, in this section, the outermost radius of the transmitter coil R_a and that of the receiver coil R_c are selected by users. Similarly, the number of turns (N_a, N_c), other geometrical parameters (t_1, t_2, z_1, z_2, d_w, c, and d), and physical parameters (μ_r, σ, and f) are also determined manually. Therefore, the design procedure can be regarded as working out the radius R_b and turn number N_b of antiparallel windings under given parameters.

Fig. 11 shows the flowchart for the design process of the magnetic coupler. The program starts with given initial values of R_b and N_b, notating as R_0 and N_0 and then increasing R_b by a little step ΔR and N_0 by 1 gradually to their maximum. The performance of design result is evaluated by the standard deviation σ of equivalent mutual inductance M_e. The lower the σ, the smaller the fluctuation of mutual inductance when misalignment occurs, and the better performance of the design. The optimization objective is the minimum σ within the misalignment l.

In this article, considering the application of drones, the parameters are designed to be compatible with the requirements of the drone DJI-MATRICE-100 as an example. Limited by the size of the drone, the geometrical parameters are selected as $R_a = 0.2$ m, $N_a = 10$, $R_c = 0.1$ m, $N_c = 20$, $z_1 = 2.6$ mm, and $z_2 = 10$ cm. The turn spaces are chosen as $t_1 = t_2 =$ 3.2 mm in order to make the system more compact. The parameters of ferrite substrate are $c = 0.2$ m, $d = 4$ mm, $\mu_r = 2300$, and $\sigma = 0.001$ S/m, which are dependent on the ferrite material used in the experiment. Similarly, d_w is 3.2 mm since the litz wire with 3.2-mm diameter is utilized in the experiment. The operating frequency is chosen as 300 kHz due to that the quality factor of the coil can be increased with a high frequency. The step $\Delta R = 0.001$ m. The landing error of the drone is 0.1 m; thus, l is set as 0.1 m. Finally, the design results are $R_{\text{best}} = 0.100$ m, $N_{\text{best}} = 3$, and $\sigma = 0.0944$ μH. The calculated, simulated, and measured mutual inductance versus misalignment is shown in Fig. 12.

The influence of antiparallel windings is reflected in the mutual inductance. For the proposed system, it maintains good stability, M_{12}, as shown in Fig. 12, while that of the traditional system without antiparallel windings shows a downward trend, M_{ac}, as shown in Fig. 12. Therefore, according to (5) and (7), the output current and power can remain stable with the help of antiparallel windings. M_{12} is lower than M_{ac}, which means the proposed system has a higher current gain. Thus, the system has a larger output power under the same input voltage, showing a larger power capability. The efficiency of the proposed system would be slightly lower than that of the traditional system due to the decline of mutual inductance. However, this drawback can be minimized by properly designing the coil. Since the antiparallel windings are designed to be small, they would merely have a little effect on efficiency.

With the measured mutual inductance in Fig. 12 and other parameters given in Section VI, the theoretical efficiency of the system can be calculated by (8), as shown in Fig. 13. It can be seen that the system can maintain a high efficiency at different load resistance and misalignment, and it can remain constant when misalignment occurs. To sum up, the antiparallel windings can bring a stable output current and power, a higher current gain and power capability, and a slightly lower but stable efficiency.

Fig. 14 shows the magnetic field distribution of the proposed magnetic coupler by Ansoft Maxwell, compared to the one without antiparallel windings. The transmitter coils are excited

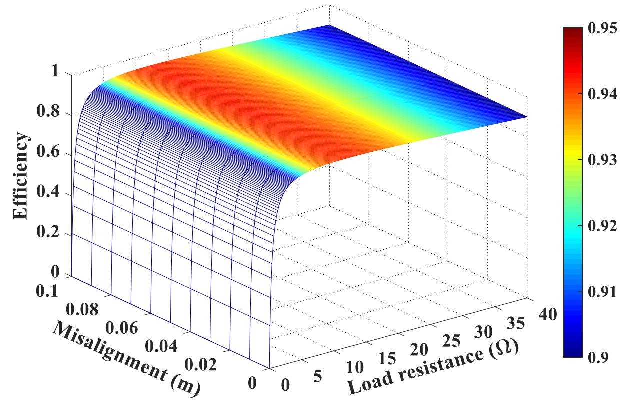

Fig. 13. Calculated efficiency of the proposed WPT system versus load resistance and misalignment.

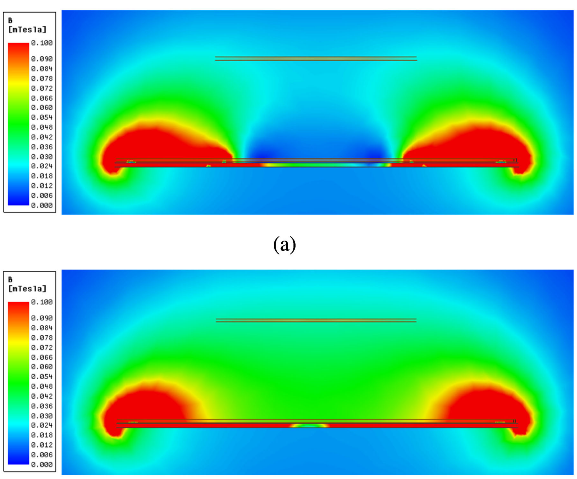

(a)

(b)

Fig. 14. Magnetic field distribution of the coupler (a) with and (b) without antiparallel windings.

by 1 A current. It can be seen from Fig. 14 that there is a little zero-magnetic-flux-density area in the proposed coupler, which illustrates the magnetic field counteracting characteristic of the proposed coupler, as stated in Section II.

VI. Experiment

A. Verification Experiment

In this section, an experimental prototype of the antimisalignment WPT system is established to verify the theoretical analysis, as shown in Fig. 15. The experimental prototype is made up of a dc voltage source, a full-bridge inverter, a magnetic coupler, a full-bridge rectifier, and a load resistance. The inverter consists of four MOSFETs (IRFP250 N), while four diodes (MBR16100CT) are utilized to compose the rectifier. The values of system parameters are shown in Table II.

The pad was designed by the methodology proposed in Section V, and the geometrical parameters are listed in Table III. Due to the difficulty in manufacturing large round ferrite, the substrate was pieced together by $54 \times 23 \times 4$ mm ferrite cuboid PC 40. Litz wire of 400 strands with the 3.2-mm diameter is

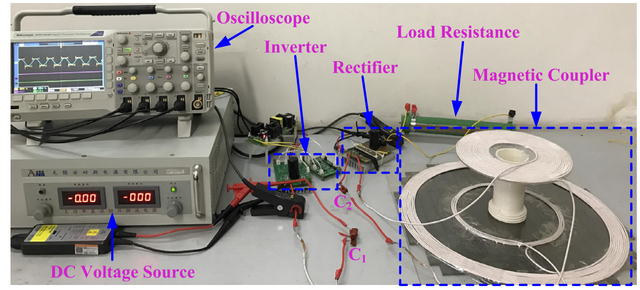

Fig. 15. Experimental prototype of the proposed WPT system.

TABLE II
System Parameters of the Experiment

Parameter	Value	Parameter	Value	Parameter	Value
L_1	112.6 μH	C_1	2.50 nF	U_{in}	60 V
L_2	64.0 μH	C_2	4.40 nF	I_{out}	3.35 A
R_p	0.56 Ω	R_s	0.30 Ω	f	300 kHz

TABLE III
Geometrical Parameters of the Designed Coil

Parameter	Value	Parameter	Value	Parameter	Value
R_a	20.0 cm	N_a	10	t_1	3.2 mm
R_b	10.0 cm	N_b	3	t_2	3.2 mm
R_c	10.0 cm	N_c	20	z_1	2.6 mm

utilized to wind the coil, which can reduce the ESR. The distance between two coils in experiment is $z_2 = 10$ cm.

Fig. 16 shows the experimental waveforms of input voltage/current and output voltage/current of the proposed system in different positions when $R_L = 20\ \Omega$. U_1' is the input voltage to the primary side, which was generated by the full-bridge inverter, and I_1 is the current of the primary side. U_{out} and I_{out} are the waveforms of output voltage and current of the rectifier, respectively, and they remain almost unchanged in all misalignment cases, which indicates that the system can achieve antimisalignment characteristic. U_1' and I_1 are of the same phase angle, since the operating frequency is set as same as the resonant frequency of the coils and capacitors. The actual operating frequency in the experiment was 292.8 kHz due to the manufacture error between the real value and the designed value among the capacitance.

B. Comparison Experiment

In order to discuss the merits and demerits of the proposed design, two groups of comparison experiments are carried out. The proposed coil design is noted as design 1, the proposed coil design without the antiparallel loop is named as design 2, and an optimized traditional pad is named as design 3. These three designs are shown in Fig. 17.

For the optimized pad (design 3), the outer radius is set as same as the proposed design, which is 20 cm. It has been proved that a smaller inner radius could always improve the magnetic coupling. When the ratio of inner and outer radii is about 0.4,

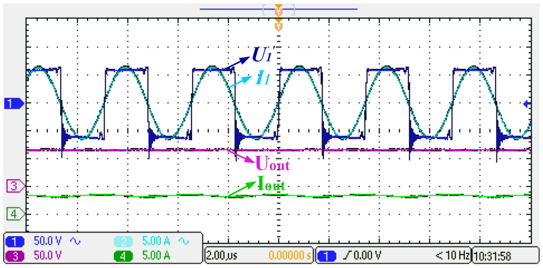

(a)

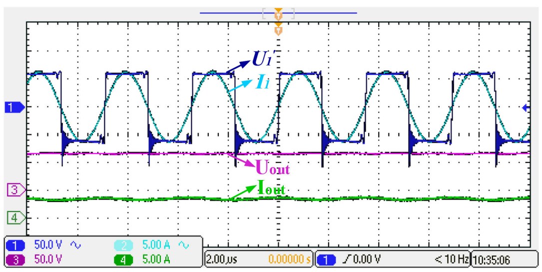

(b)

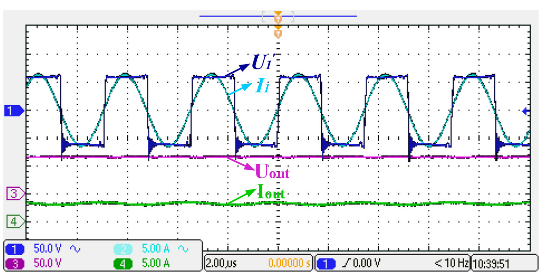

(c)

Fig. 16. Experimental waveforms of U_1, I_1, U_{out}, and I_{out} when $R_L = 20\,\Omega$. (a) Well aligned. (b) 0.05-m misalignment. (c) 0.1-m misalignment.

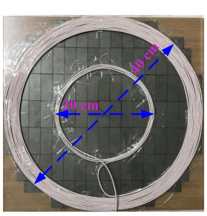

(a)

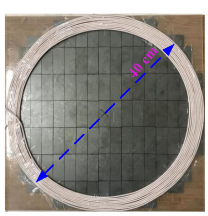

(b)

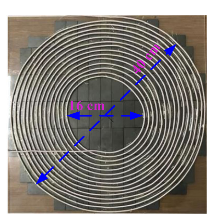

(c)

Fig. 17. View of different pads. (a) Design 1. (b) Design 2. (c) Design 3.

the system would have the best coupling factor [39]. Therefore, the inner radius of design 3 is approximately 8 cm. In [39], it is shown that for the single-layer spiral coil, the magnetic coupling is only affected by the outer and inner diameter. The conductor diameter, the separation of the conductors, and the number of turns could be chosen arbitrarily if the inner and outer radii are constant. To have a better comparison, the self-inductance of design 3 is set roughly equal to that of designs 1 and 2. Therefore, the number of turns is set as 14, and wires are equally separated in the area.

The self-inductances of these three designs are 112.6, 110.0, and 110.8 μH, respectively. Other experimental parameters are the same as those in Table II. The load resistance is $R_L = 20\,\Omega$. The measured coupling coefficients and overall efficiency are

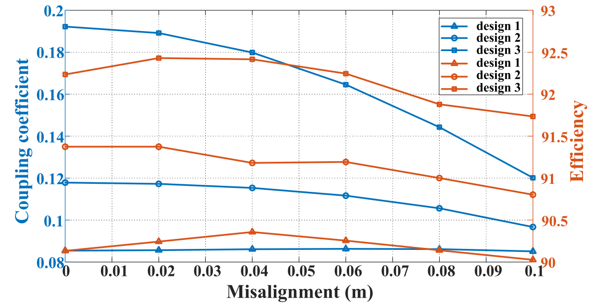

Fig. 18. Comparison of coupling coefficients and system efficiency.

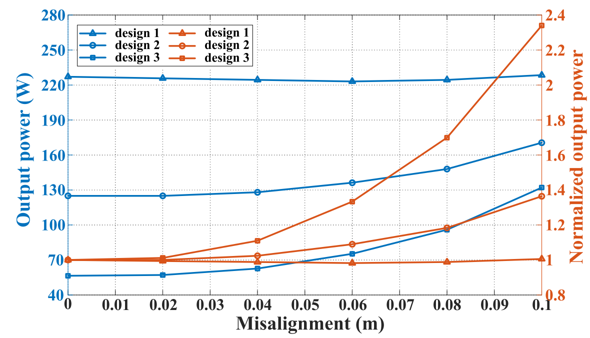

Fig. 19. Comparison of output power and its normalized value.

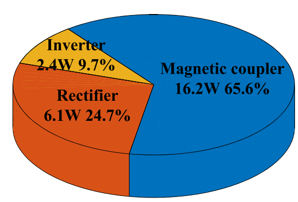

Fig. 20. System loss distribution chart at 0.1-m misalignment when $R_L = 20\,\Omega$.

shown in Fig. 18. The output power and its normalized value of each design are shown in Fig. 19.

Fig. 18 illustrates that the coupling coefficient and efficiency of the proposed system can basically remain stable. The efficiency is above 90.2% within a 0.1-m misalignment. However, compared to the two traditional designs, the coupling coefficient is lower in each position, which leads to the efficiency of the proposed system a little bit lower than that of the traditional system in all cases. However, the antiparallel windings only have a small effect on system efficiency, since they are designed to be very small.

Fig. 19 shows that the output power of the proposed design has a good stability. The output power can remain constant when misalignment occurs, while that of the traditional system changes significantly due to the decline of mutual inductance. Without antiparallel windings, the output power changes by 40% at 0.1-m misalignment. In the meantime, the output power of the optimized system increases to 140%. Besides, the proposed system has a higher output gain, the output power is higher than that of traditional design at each position.

The power loss distribution of the system at 0.1-m misalignment is shown in Fig. 20. Since the output current/power and

TABLE IV
COMPARISON BETWEEN THE STATE-OF-THE-ART WORK AND THIS ARTICLE

Method		Maximum Efficiency	Output Power	Misalignment Tolerance	Constant Power	Cost	Direction
Control Scheme	[8] Phase-shift control	95.1%	1 kW	25%(20 cm/80 cm)	Yes	High	Single
	[11] PID control	85%	1 kW	15%	Yes	High	Single
Compensation Topology	[15] Hybrid LCC-LCC/SS	91.1%	3 kW	21.7%(16 cm/73.8 cm)	Yes	High	Single
	[17] Hybrid LCC-S/S-LCC	92.5%	1 kW	25%(10 cm/40 cm)	Yes	High	Single
	[18] One-to-two topology	86%	90 W	\	No	High	Single
Coil Structure	[20] DD pad	\	1921 W	\	No	Medium	Single
	[22] Bipolar pad	\	1600 W	\	No	Medium	Single
	[23] Taichi pad	80.1%	101.6 W	17.9% (5 cm/28 cm)	No	Low	Single
	[This work] Anti-parallel pad	90.7%	227.1 W	25% (10 cm/40 cm)	Yes	Low	All

efficiency in each misaligned case are almost the same, the loss distribution is approximately the same as well. The power loss of the magnetic coupler accounts for the majority of the total loss.

To sum up, the addition of antiparallel windings slightly reduces system efficiency, but the output stability is improved dramatically. The proposed method is useful in improving misalignment tolerance. The comparisons between state-of-the-art work and this article are listed in Table IV.

VII. CONCLUSION

This article proposes a novel all-direction antimisalignment WPT system by using antiparallel windings. A thorough mathematical model of the proposed system is established to illustrate the realization of high misalignment tolerance in theory. The antimisalignment characteristic is the inherent property of the magnetic coupler, which does not rely on the compensation topologies and control schemes. According to the newly designed coils, the mutual inductance can remain constant when misalignment occurs; thus, the output power can remain stable as well. Furthermore, a novel analytical method to calculate mutual inductance with a finite ferrite substrate based on the TREE method is proposed. It improves and simplifies the coil design process, which is dependent on FEA software in previous research. Finally, experiments have been carried out to verify the correctness and feasibility of the system. The system can keep a 7.2-μH mutual inductance among 0.1-m misalignment. The efficiency is above 90.2% in all cases, and the fluctuation of the output power is within 3%. The system can be widely used in EVs and UAVs.

REFERENCES

[1] Z. Zhen, H. Pang, A. Georgiadis, and C. Cecati, "Wireless power transfer—An overview," *IEEE Trans. Ind. Electron.*, vol. 66, no. 2, pp. 1044–1058, Feb. 2019.

[2] S. Ping, A. P. Hu, S. Malpas, and D. Budgett, "A frequency control method for regulating wireless power to implantable devices," *IEEE Trans. Biomed. Circuits Syst.*, vol. 2, no. 1, pp. 22–29, Mar. 2008.

[3] Z. Yan, Q. Siyao, Q. Zhu, L. Huang, and A. P. Hu, "A simple brightness and color control method for LED lighting based on wireless power transfer," *IEEE Access*, vol. 6, pp. 51 477–51483, 2018.

[4] D. H. Tran, V. B. Vu, and W. Choi, "Design of a high efficiency wireless power transfer system with intermediate coils for the on-board chargers of electric vehicles," *IEEE Trans. Power Electron.*, vol. 33, no. 1, pp. 175–187, Jan. 2018.

[5] H. Fukuda, N. Kobayashi, K. Shizuno, S. Yoshida, M. Tanomura, and Y. Hama, "New concept of an electromagnetic usage for contactless communication and power transmission in the ocean," in *Proc. IEEE Int. Underwater Technol. Symp.*, Mar. 2013, pp. 1–4.

[6] T. Long, M. Ozger, O. Cetinkaya, and O. B. Akan, "Energy neutral internet of drones," *IEEE Commun. Mag.*, vol. 56, no. 1, pp. 22–28, Jan. 2018.

[7] J. P. K. Sampath, A. Alphones, and D. M. Vilathgamuwa, "Figure of merit for the optimization of wireless power transfer system against misalignment tolerance," *IEEE Trans. Power Electron.*, vol. 32, no. 6, pp. 4359–4369, Jun. 2017.

[8] Y. Liu, U. K. Madawala, R. Mai, and Z. He, "Zero-phase-angle controlled bidirectional wireless EV charging systems for large coil misalignments," *IEEE Trans. Power Electron.*, vol. 35, no. 5, pp. 5343–5353, May 2020.

[9] Y. Liu, U. K. Madawala, R. Mai, and Z. He, "Control of wireless power transfer systems under large coil misalignments," in *Proc. IEEE 15th Brazilian Power Electron. Conf./5th IEEE Southern Power Electron. Conf.*, 2019, pp. 1–4.

[10] F. F. Van Der Pijl, M. Castilla, and P. Bauer, "Adaptive sliding-mode control for a multiple-user inductive power transfer system without need for communication," *IEEE Trans. Ind. Electron.*, vol. 60, no. 1, pp. 271–279, Jan. 2013.

[11] M. J. Neath, A. K. Swain, U. K. Madawala, and D. J. Thrimawithana, "An optimal PID controller for a bidirectional inductive power transfer system using multiobjective genetic algorithm," *IEEE Trans. Power Electron.*, vol. 29, no. 3, pp. 1523–1531, Mar. 2014.

[12] J. L. Villa, J. Sallan, J. F. S. Osorio, and A. Llombart, "High-misalignment tolerant compensation topology for ICPT systems," *IEEE Trans. Ind. Electron.*, vol. 59, no. 2, pp. 945–951, Feb. 2012.

[13] J. Hou, Q. Chen, S. Wong, C. K. Tse, and X. Ruan, "Analysis and control of series/series-parallel compensated resonant converter for contactless power transfer," *IEEE Trans. Emerg. Sel. Topics Power Electron.*, vol. 3, no. 1, pp. 124–136, Mar. 2015.

[14] H. Feng, T. Cai, S. Duan, J. Zhao, X. Zhang, and C. Chen, "An LCC-compensated resonant converter optimized for robust reaction to large coupling variation in dynamic wireless power transfer," *IEEE Trans. Ind. Electron.*, vol. 63, no. 10, pp. 6591–6601, Oct. 2016.

[15] L. Zhao, D. J. Thrimawithana, and U. K. Madawala, "Hybrid bidirectional wireless EV charging system tolerant to pad misalignment," *IEEE Trans. Ind. Electron.*, vol. 64, no. 9, pp. 7079–7086, Sep. 2017.

[16] L. Zhao, S. Ruddell, D. J. Thrimawithana, U. K. Madawala, and P. A. Hu, "A hybrid wireless charging system with DDQ pads for dynamic charging of EVS," in *Proc. IEEE PELS Workshop Emerg. Technol.: Wireless Power Transfer*, 2017, pp. 1–6.

[17] Y. Chen, B. Yang, Z. Kou, Z. He, G. Cao, and R. Mai, "Hybrid and reconfigurable IPT systems with high-misalignment tolerance for constant-current and constant-voltage battery charging," *IEEE Trans. Power Electron.*, vol. 33, no. 10, pp. 8259–8269, Oct. 2018.

[18] J. Chen *et al.*, “Free-positioning wireless power transfer system based on one-to-multiple topology,” *IEEE Trans. Power Electron.*, vol. 35, no. 10, pp. 9959–9964, Oct. 2020.
[19] J. W. Kim *et al.*, “Wireless power transfer for free positioning using compact planar multiple self-resonators,” in *Proc. IEEE MTT-S Int. Microw. Workshop Ser. Innov. Wireless Power Transmiss.: Technol., Syst., Appl.*, 2012, pp. 127–130.
[20] M. Budhia, J. T. Boys, G. A. Covic, and C. Huang, “Development of a single-sided flux magnetic coupler for electric vehicle IPT charging systems,” *IEEE Trans. Ind. Electron.*, vol. 60, no. 1, pp. 318–328, Jan. 2013.
[21] G. Ke, Q. Chen, W. Gao, S. Wong, and C. K. Tse, “Power converter with novel transformer structure for wireless power transfer using a DD2Q power receiver coil set,” in *Proc. IEEE Energy Convers. Congr. and Expo.*, 2016, pp. 1–6.
[22] G. A. Covic, M. L. G. Kissin, D. Kacprzak, N. Clausen, and H. Hao, “A bipolar primary pad topology for EV stationary charging and highway power by inductive coupling,” in *Proc. IEEE Energy Convers. Congr. Expo.*, 2011, pp. 1832–1838.
[23] Y. Li, J. Zhao, Q. Yang, L. Liu, J. Ma, and X. Zhang, “A novel coil with high misalignment tolerance for wireless power transfer,” *IEEE Trans. Magn.*, vol. 55, no. 6, pp. 1–4, Jun. 2019.
[24] J. T. Conway, “Inductance calculations for noncoaxial coils using bessel functions,” *IEEE Trans. Magn.*, vol. 43, no. 3, pp. 1023–1034, Mar. 2007.
[25] W. G. Hurley and M. C. Duffy, “Calculation of self- and mutual impedances in planar sandwich inductors,” *IEEE Trans. Magn.*, vol. 33, no. 3, pp. 2282–2290, May 1997.
[26] Z. Luo and X. Wei, “Analysis of square and circular planar spiral coils in wireless power transfer system for electric vehicles,” *IEEE Trans. Ind. Electron.*, vol. 65, no. 1, pp. 331–341, Jan. 2018.
[27] W. G. Hurley and M. C. Duffy, “Calculation of self and mutual impedances in planar magnetic structures,” *IEEE Trans. Magn.*, vol. 31, no. 4, pp. 2416–2422, Jul. 1995.
[28] Y. P. Su, X. Liu, and S. Y. R. Hui, “Mutual inductance calculation of movable planar coils on parallel surfaces,” *IEEE Trans. Power Electron.*, vol. 24, no. 4, pp. 1115–1123, Apr. 2009.
[29] T. Theodoulidis and E. Kriezis, *Eddy Current Canonical Problems (With Applications to Nondestructive Evaluation)*. Forsyth, GA, USA: Tech Sci. Press, 2006.
[30] T. Theodoulidis and J. Bowler, “The truncated region eigenfunction expansion method for the solution of boundary value problems in eddy current nondestructive evaluation,” *AIP Conf. Proc.*, vol. 760, pp. 403–408, 2005.
[31] Z. Dong, S. Liu, X. Li, Z. Xu, and L. Yang, “A novel long-distance wireless power transfer system with constant current output based on domino-resonator,” *IEEE Trans. Emerg. Sel. Topics Power Electron.*, vol. 9, no. 2, pp. 2343–2355, Apr. 2021.
[32] K. Song, Z. Li, J. Jiang, and C. Zhu, “Constant current/voltage charging operation for series-series and series-parallel compensated wireless power transfer systems employing primary-side controller,” *IEEE Trans. Power Electron.*, vol. 33, no. 9, pp. 8065–8080, Sep. 2018.
[33] Y. Lei, *Analytical Method of Time Harmonic Electromagnetic Field*. Beijing, China: Science Press, 2000.
[34] C. V. Dodd and W. E. Deeds, “Analytical solutions to eddy-current probe-coil problems,” *J. Appl. Phys.*, vol. 39, no. 6, pp. 2829–2838, 1968.
[35] P. Morse and H. Feshbach, *Methods of Theoretical Physics*. New York, NY, USA: McGraw-Hill, 1955.
[36] D. Yao, *Methods of Mathematical Physics*. Beijing, China: Science Press, 2010.
[37] A. K. RamRakhyani, S. Mirabbasi, and M. Chiao, “Design and optimization of resonance-based efficient wireless power delivery systems for biomedical implants,” *IEEE Trans. Biomed. Circuits Syst.*, vol. 5, no. 1, pp. 48–63, Feb. 2011.
[38] Z. Pantic and S. Lukic, “Computationally-efficient, generalized expressions for the proximity-effect in multi-layer, multi-turn tubular coils for wireless power transfer systems,” *IEEE Trans. Magn.*, vol. 49, no. 11, pp. 5404–5416, Nov. 2013.
[39] R. Bosshard, J. W. Kolar, J. Mühlethaler, I. Stevanović, B. Wunsch, and F. Canales, “Modeling and η-α-pareto optimization of inductive power transfer coils for electric vehicles,” *IEEE Trans. Emerg. Sel. Topics Power Electron.*, vol. 3, no. 1, pp. 50–64, Mar. 2015.

Zifan Dong received the B.S. degree in 2019 from the College of Electrical Engineering and Automation, Wuhan University, Wuhan, China, where he is currently working toward the M.S. degree.

His main research interests include wireless power transfer.

Xiaoming Li received the B.S. and M.Sc. degrees in electrical engineering and automation from Wuhan University, Wuhan, China, in 1978 and 1986, respectively, and the Ph.D. degree from the Huazhong University of Science and Technology, Wuhan, in 2000.

He is currently a Professor with the College of Electrical Engineering and Automation, Wuhan University. His research interests include wireless power transfer, power system operation and control, application of power electronics technology in power systems, and smart grids.

Sheng Liu received the B.S. and M.S. degrees from the College of Electrical Engineering and Automation, Wuhan University, Wuhan, China, in 2017 and 2020, respectively. He is currently working toward the Ph.D. degree with the College of Electrical Engineering, Zhejiang University, Hangzhou, China.

His main research interests include wireless power transfer.

Ziwei Xu received the B.S. degree from the College of Energy and Electrical Engineering, Hohai University, Nanjing, China, in 2018. She is currently working toward the M.S. degree with the College of Electrical Engineering and Automation, Wuhan University, Wuhan, China.

Her main research interests include wireless power transfer.

Lin Yang received the Ph.D. degree from the College of Electrical Engineering and Automation, Wuhan University, Wuhan, China, in 2020.

He is currently a Lecturer with the College of Electronic and Electrical Engineering, Henan Normal University, Xinxiang, China. His research interests include wireless power transfer technology, resonant converters, and magnetic coupler design.